

Probing Atomic-Scale Processes at the Ferrihydrite-Water Interface With Reactive Molecular Dynamics

Ardalan Hayatifar,^{*,†} Simon Gravelle,[‡] Beatriz D. Moreno,[¶] Valerie A. Schoepfer,[†]
¹ and Matthew B.J. Lindsay^{*,†}

[†]*Department of Geological Sciences, University of Saskatchewan, Saskatoon, SK, Canada
S7N 5E2*

[‡]*University Grenoble Alpes, CNRS, LIPhy, 38000 Grenoble, France*

[¶]*Brockhouse Diffraction Sector, Canadian Light Source, Saskatoon, SK, Canada*

E-mail: ardalan.hayatifar@usask.ca; matt.lindsay@usask.ca

2 **Abstract**

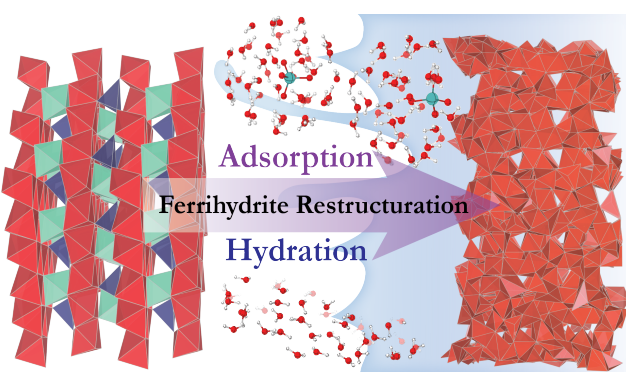
3 Interfacial processes involving metal (oxyhydr)oxide phases are important for the
4 mobility and bioavailability of nutrient and contaminant elements in soils, sediments,
5 and water. Consequently, these processes influence ecosystem health and functioning,
6 and have shaped the biological and environmental co-evolution of Earth over geologic
7 time. Here we employ reactive molecular dynamics simulations, supported by syn-
8 chrotron X-ray spectroscopy to study the molecular-scale interfacial processes that in-
9 fluence surface complexation in ferrihydrite-water systems containing aqueous MoO_4^{2-} .
10 We validate the utility of this approach by calculating surface complexation models di-
11 rectly from simulations. The reactive force-field captures the realistic dynamics of
12 surface restructuring, surface charge equilibration, and the evolution of the interfacial
13 water hydrogen bond network in response to adsorption and proton transfer. We find
14 that upon hydration and adsorption, ferrihydrite restructures into a more disordered
15 phase through surface charge equilibration, as revealed by simulations and grazing inci-
16 dent X-ray scattering. We observed how this restructuring leads to a different interfacial
17 hydrogen bond network compared to bulk water by monitoring water dynamics. Us-
18 ing umbrella sampling, we constructed the free energy landscape of aqueous MoO_4^{2-}
19 adsorption at various concentrations and the deprotonation of the ferrihydrite surface.
20 The results demonstrate excellent agreement with the values reported by experimen-
21 tal surface complexation models. These findings are important as reactive molecular
22 dynamics opens new avenues to study mineral-water interfaces, enriching and refining
23 surface complexation models beyond their foundational assumptions.

24 **Keywords**

25 Adsorption, Umbrella Sampling, Synchrotron X-ray, Pair Distribution Function, Surface
26 Complexation Models, Ferrihydrite

²⁷ TOC Art

²⁸



²⁹ Introduction

The mobility and bioavailability of nutrient and contaminant elements in soils, sediments and water are strongly influenced by atomic-scale processes at mineral-water interfaces. Surface adsorption or precipitation reactions can promote element attenuation, while desorption and dissolution reactions may drive element release^{1–3}. Ferrihydrite (Fh) and other iron (oxyhydr)oxides are often important controls on aqueous concentrations of oxyanion-forming elements, which can have important implications for ecosystem health and functioning^{4–6}. For example, molybdate (MoO_4^{2-}) adsorption onto Fh surfaces has implications for biosynthesis of Mo-enzymes central to global biogeochemical cycles that have shaped Earth's biological and environmental coevolution.

In aqueous systems, Fh typically bears a non-zero surface charge originating from the ionization of the surface hydroxyl ($-\text{OH}$) groups and the adsorption of dissolved ions^{7,8}. Oxyanions adsorption strongly influences physical, chemical, and structural properties of the Fh surface^{9,10}, primarily due to the induced re-organizing of water molecules altering phase stability and its transformation pathways¹¹. Furthermore, Fh surface charge modification through adsorption not only leads to a reorientation of interfacial species, affecting both their adsorption kinetics and diffusion across the interface but also alters the hydrogen bond (HB) network at the interface. This alteration in the HB network additionally influences

47 the acidity of protic species, which include any species capable of donating a hydrogen ion
48 (H^+)^{8,12,13}.

49 Past studies of charged interfaces in water experiencing adsorption events have com-
50 monly relied on empirical studies, supported by various spectroscopic techniques and surface
51 complexation models (SCM), while some recent studies have used more advanced method-
52 ologies^{7,14–19}. SCM account for surface charge along with solute-surface adsorption complex
53 equilibrium constants to fit a model of surface complexes to batch adsorption experiments
54 data^{20,21}. The models rely upon empirical constants to describe the equilibrium between
55 aqueous species and mineral surface sites^{22,23} using parameters such as surface site den-
56 sity, surface potential, intrinsic acid-base constants, and apparent complexation constants,
57 determined with the assistance of non-linear parameter estimation codes^{23–25}.

58 While SCM have proven valuable, they require fitting a large amount of data under the
59 presumption that surfaces are static and homogeneous^{25–28}, and simplifying the effects of wa-
60 ter chemistry^{15,29–31}. Reactive molecular dynamics (MD) simulations offer a complementary
61 perspective by providing a realistic depiction of fluid-solid interactions. Reactive force fields
62 such as ReaxFF allow one to simulate molecular dynamics while incorporating bond-breaking
63 and formation events. They are more computationally efficient than *ab initio* MD^{19,32,33} and
64 density functional theory (DFT) methods for the Mo(VI)- FeO_x interface^{19,34,35}. Reactive
65 force-fields have proven successful in modeling solid-water interfaces³⁶, accurately describing
66 the restructuration of clay surfaces and interlayers in water consistent with neutron scat-
67 tering and nuclear magnetic resonance spectroscopy (NMR) data³⁷. Furthermore, reactive
68 force fields have been utilized to examine the reactions of water with solid surfaces. This
69 includes describing reactivity trends of various crystal surfaces towards water dissociation in
70 TiO_2 ³⁸, and studying water dissociation at the surfaces of calcium silicate hydrate micropores
71 and silica surfaces, successfully reproducing experimental properties, such as dipole moment,
72 diffusion coefficients, and proton-transfer pathways similar to the Grotthuss mechanism^{39,40}.

73 Here, we use reactive MD paired with synchrotron X-ray scattering to explore processes

74 at the Fh-water interface, surface restructuring during aqueous MoO_4^{2-} adsorption. Our
75 results also explore the surface charge of Fh and interfacial HB network. Additionally, we
76 leverage our model to calculate SCM constants from simulations using umbrella sampling,
77 achieving excellent agreement for surface acidity and the concentration-dependent adsorp-
78 tion constants of MoO_4^{2-} . Our approach effectively integrates experimental findings with
79 theoretical models⁴¹, particularly in connecting MD simulations to empirical SCM parame-
80 ters.

81 The choice of molybdenum in its aqueous molybdate form (MoO_4^{2-}) as a model oxyanion
82 is motivated by its dual role as an essential micronutrient and a pollutant element^{42,43}.
83 Bioavailable molybdenum is crucial in the function of oxidoreductase enzymes within the
84 biogeochemical cycles of N, C, and S. Furthermore, mobile aqueous molybdenum species
85 negatively impact water quality, underscoring its significant environmental and biological
86 implications.

87 The choice of molybdenum in its aqueous molybdate form (MoO_4^{2-}) as a model oxyanion
88 is motivated by its importance as an essential micronutrient and a pollutant element^{42,43}.
89 Bioavailable molybdenum has a critical role in the function of oxidoreductase enzymes within
90 the biogeochemical cycles of N, C, and S. Additionally, mobile aqueous molybdenum species
91 have a negative impact on water quality, reflecting the environmental and biological relevance
92 of our findings.

93 Materials and Methods

94 Sample Preparation

95 Synthesis of 2-line Fh followed the method of Schwertmann and Cornell⁴⁴, where 500 mL of
96 a 0.2 M $\text{Fe}(\text{NO}_3)_3 \cdot 9\text{H}_2\text{O}$ solution was titrated to approximately pH 7.5 using 1 M KOH.
97 The base addition was conducted over approximately 30 minutes and the resulting solution
98 was stirred for approximately 1 hour. Aliquots of the suspension were transferred into 50

⁹⁹ mL conical tubes, which were centrifuged at 3000 rpm for 5 minutes. The supernatant was
¹⁰⁰ decanted and 40 mL ultrapure water was added and mixed. The centrifugation process and
¹⁰¹ ultrapure water addition was repeated for a total of three times to remove residual salts.
¹⁰² Solids were flash frozen and freeze dried, and powder X-ray diffraction confirmed phase
¹⁰³ identity.

¹⁰⁴ Modeling Setup

¹⁰⁵ Fh slabs and surfaces were generated based on the structure suggested by Michel *et al.*⁴⁵.
¹⁰⁶ The Fh supercell was terminated by oxygen atoms of (1̄10) plane, which accounts for 67-85,
¹⁰⁷ % of the total surface area of Fh⁴⁶, to emulate geochemical conditions, using Pymatgen⁴⁷.
¹⁰⁸ Symmetric slab with zero or no dipole moment was then selected for the preparation of 3.6
¹⁰⁹ × 3.5 × 2.9 nm Fh supercell, with the composition of Fe_{946.56}H₁₄₄O₁₅₃₆. Dangling surface
¹¹⁰ oxygens were saturated by hydrogen atoms based on their acidity.

¹¹¹ Reactive MD Simulations

¹¹² All simulations were carried out with LAMMPS package⁴⁸ using the ReaxFF *pair_style* as
¹¹³ implemented in LAMMPS⁴⁹, with the ReaxFF parameters obtained for Fh⁵⁰, Mo⁵¹, Na⁵²,
¹¹⁴ and Na–Fe cross-terms⁵³. The data files for simulations were prepared using the VMD
¹¹⁵ TopoTools plugin and Moltemplate^{54,55}. Except in the microcanonical ensemble (*NVE* -
¹¹⁶ constant number of atoms, volume, and energy) where a Berendsen thermostat was utilized,
¹¹⁷ in all other cases Nosé-Hoover thermostat and barostat with damping constants of 100
¹¹⁸ fs, and 1000 fs were used to control the temperature and pressure, respectively. In all
¹¹⁹ simulations, a time step of 0.25 fs was used to integrate Newton's equation of motion by the
¹²⁰ velocity-Verlet algorithm. The charge polarization effects of all atoms were included in the
¹²¹ simulation by calculating geometry-dependent atomic charges at every time step using the
¹²² charge equilibration (*QE**q*) approach with a cutoff radii 10.0 Å for all interactions⁵⁶.

¹²³ The initial configuration of the slab was first minimized using the steepest descent algo-

124 rithm while stopping tolerances for energy and force were set to 10^{-4} and 10^{-6} ($\text{kcal} \cdot \text{mol}^{-1} \cdot \text{\AA}^{-1}$),
125 respectively. To prevent melting, the temperature of the system was gradually increased in
126 a series of iterations in the *NVT* ensemble, starting with 10,000 steps of 0.1 Å maximum
127 distance-limited *NVE* (*nve/limit* in LAMMPS) at 1 K (damping constant 1 fs), followed
128 by *NVT* stages consisting of 10,000 steps at 1 K (damping constant 1 fs) and a 10,000
129 steps temperature ramp from 1 K to 300 K (damping constant 100 fs). Finally, the slab
130 was relaxed for 1 ns in the anisotropic *NPT* ensemble (constant number of atoms, pressure,
131 and temperature) at 298 K and 1 atm in *x* and *y* directions in a simulation cell with the
132 dimensions of approximately $4 \times 4 \times 6.7$ nm including a 4 nm gap in the *z* direction, in
133 which the volume was subsequently filled with equilibrated aqueous solutions.

134 The initial configuration of solutions was prepared by randomly placing aqueous ions
135 within the 3.0 Å region of the middle of the bulk aqueous solution to yield simulations
136 of Fh and solutions containing different numbers of Na_2MoO_4 (Mo-n, n= 0, 1, 2, 3, 6,
137 8), corresponding to $[\text{Na}_2\text{MoO}_4] = 0, 0.025, 0.05, 0.075, 0.15,$ and $0.2 \text{ (mol.L}^{-1}\text{)}$ with a
138 water density of 33 (*particle.nm*⁻³) using Packmol⁵⁷. In the equilibration stage, solutions
139 were first simulated while turning off ReaxFF mechanism. This was achieved by treating
140 water O–H and molybdate Mo–O bonds as classical harmonic springs with a constant
141 of 50 ($\text{kcal} \cdot \text{mol}^{-1} \cdot \text{\AA}^{-2}$). The spring constant was chosen considering the ef activeness of
142 pressure/temperature control and the stability of simulations with the used time step⁵⁸. The
143 equilibration of solutions while water O–H and molybdate Mo–O bonds were constrained
144 using harmonic restraints, was performed for 0.2 ns, divided into stages comprising of 100 ps
145 of 0.1 Å maximum distance-limited *NVE* at 298 K (damping constant 100 fs), 100 ps in the
146 *NVE* 298 K (damping constant 50 fs), 300 ps in the canonical ensemble (*NVT* - constant
147 number of atoms, volume, and temperature) at 298 K (damping constant 50 fs), and 500
148 ps in the *NPT* at 298 K and 1 atm in *z* direction. For each concentration, 3 independent
149 simulations have been performed to capture statistical variations. The reactive simulations
150 for all reps are then combined and used for further analysis using in house python codes

¹⁵¹ based on MDAnalysis package^{59,60}.

¹⁵² Umbrella Sampling

¹⁵³ Umbrella sampling is a technique that enables sampling of high-energy states, also known
¹⁵⁴ as rare events, that are otherwise not feasible for direct sampling⁶¹ during simulations. It
¹⁵⁵ acts by enforcing an external harmonic restraint along a reaction coordinate, in a series
¹⁵⁶ of windows, represented by a collective variable, which, in this case, is the distance of Mo
¹⁵⁷ from the surface. This free energy along the collective variable is also referred to as the
¹⁵⁸ potential-of-mean-force (PMF).

¹⁵⁹ We used Colvars module interfaced with LAMMPS to perform umbrella sampling⁶². A
¹⁶⁰ series of 20 initial configurations (windows) were generated from 0 to 20 Å from the surface
¹⁶¹ in the *z* direction (width = 1 Å). A constraining force constant of 5 Kcal.mol⁻¹.Å⁻² was
¹⁶² used, while allowing the selected Mo atom to move in *x* and *y* directions. The selected force
¹⁶³ constant resulted in sufficient overlap of the position histograms (shown in Figure SI 20),
¹⁶⁴ allowing a smooth reconstruction of the PMF. Each window was run in NVT ensemble for
¹⁶⁵ at least 3 ns. The PMFs were obtained using an algorithm known as WHAM (Weighted
¹⁶⁶ Histogram Analysis Method) which is used to remove the biasing potential and reconstruct
¹⁶⁷ the PMF with error analysis performed using the Monte Carlo bootstrap method^{63,64}.

¹⁶⁸ Synchrotron X-ray Measurements

¹⁶⁹ All X-ray measurements were conducted at Brockhouse Diffraction Sector (BXDS) at the
¹⁷⁰ Canadian Light Source (CLS). The high-resolution X-ray diffraction (XRD) data were col-
¹⁷¹ lected at Low Energy Wiggler Beamline (WLE) at the CLS. The measurements were con-
¹⁷² ducted by using a Kapton capillary filled with solid particles or particle dispersions. The
¹⁷³ capillary was mounted and spun during the measurements to improve uniformity. A fixed
¹⁷⁴ photon energy $\lambda=0.819$ Å with a Si (111) monochromator and Dectris Mythen2 X series 1K
¹⁷⁵ detector system were used.

¹⁷⁶ Pair distribution function (PDF) measurements were performed at the High Energy Wig-
¹⁷⁷ gler (HEW) beamline (Energy range 20–94 keV; beam size 2–10 mm × ~100 mm (W × H);
¹⁷⁸ energy resolution $1 \times 10^{-3} \Delta d/d$) at 54 keV (0.2265 Å) with a crystal Si (111) monochroma-
¹⁷⁹ tor. The samples were loaded in Kaptoncapillary tubes and were spun during the measure-
¹⁸⁰ ments to improve uniformity. A fixed photon energy $\lambda=0.819$ Å with a Si (111) monochro-
¹⁸¹ mator and Dectris Mythen2 X series 1K detector system were used. The data processing was
¹⁸² calibrated using a Ni standard. The data was integrated from 2D to 1D using GSAS-II⁶⁵,
¹⁸³ and the PDFs were generated by the Fourier transform of total scattering structure factor
¹⁸⁴ $S(Q)$ with a Q_{max} of 22 Å⁻¹. The PDF of containers were measure for background signal
¹⁸⁵ removal.

¹⁸⁶ Calculations of X-ray Scattering

¹⁸⁷ For XRD calculation, the thermal disorder was taken into account by averaging snapshots
¹⁸⁸ from MD trajectories separated by a 1 ps time step. To further enhance the interfacial signal,
¹⁸⁹ and emulate the experimental setup, the snapshots were limited to the interfacial region
¹⁹⁰ found by identification of truly interfacial molecules (ITIM) algorithm. XRD patterns were
¹⁹¹ simulated at $\lambda=0.819$ Å with parameters for Fe(III) and Mo(VI)⁶⁶ using *XrDebye* module of
¹⁹² Atomic Simulation Environment (ASE) package⁶⁷. The PDF plots of selected MD snapshots
¹⁹³ were calculated from atomic coordinates using the Debye scattering equation implemented
¹⁹⁴ in *Diffpy-CMI* as *DebyeCalculator* class⁶⁸. Differential pair distribution functions (d-PDFs)
¹⁹⁵ were calculated by subtracting a scaled reference PDF, Fh-water mixture from the PDF of
¹⁹⁶ Fh-[Mo]_{aq}.

¹⁹⁷ **Results and Discussion**

¹⁹⁸ **Synchrotron X-ray Spectroscopy and Reactive Molecular Dynamics**

¹⁹⁹ The grazing-incident X-ray scattering (GIXS) experiments and ensemble-averaged MD simu-
²⁰⁰ lated XRD patterns (Figure 1) for synthesized Fh (a3) and MD-relaxed Fh slab (a2) display
²⁰¹ poorly resolved, broad features suggesting the presence of 2-line nano-crystalline Fh with
²⁰² a small domain size (<10 nm), consistent with PDF data^{69,70}. Based on simulated XRD
²⁰³ patterns and radial distribution function (RDF) (Figure SI 3), MD relaxation of the initial
²⁰⁴ structure of Fh slab for MD simulations based on the Michel model⁷⁰ (a1), results in the
²⁰⁵ loss of long-range order to yield a Fh phase (a2) that closely resembles the experimental Fh
²⁰⁶ sample (a3).

²⁰⁷ Fh restructures in response to contact with water, which is evident in the XRD patterns
²⁰⁸ of both synthesized (b2) and simulated Fh (b1). These patterns exhibit increased broadening
²⁰⁹ and disorder compared to their respective *dry* structures. Upon the introduction of [Mo]_{aq},
²¹⁰ further adsorption-induced structural changes are observed, characterized by an increased
²¹¹ structural disorder in the lower angle region, particularly around $\sim 10^\circ 2\theta$ as seen in (c1).
²¹² This corresponds to the dominant surface (1̄10) plane of Fh (a2) at $10.50^\circ 2\theta$.

²¹³ The size of coherent scattering domains⁶⁹ determined by PDF signal attenuation of the
²¹⁴ Fh/water/MoO_{4(aq)} samples (Figure SI 5) suggests average crystallite size of 1.5-2 nm. The
²¹⁵ addition of water and molybdate did not produce a noticeable change in the PDF signal.
²¹⁶ The observed distances at 1.98 Å, and 3.06 Å align closely with the reported values of 2 Å
²¹⁷ for the Fe–O bond in tetrahedrally coordinated iron and 3.03 Å for the Fe–Fe bond in FeO₆
²¹⁸ polyhedra⁶⁹.

²¹⁹ The d-PDF (c-b), comprising of peaks at 1.98, 3.10, and 3.43 Å (Figure 2-A), enhances
²²⁰ interfacial signals by isolating the interfacial region from the bulk system. This focus on
²²¹ changes in the PDF of Fh/water introduced by [Mo]_{aq} allows for a more detailed analysis
²²² of interfacial interactions. The simulation of the PDF from the Mo-9 trajectory, containing

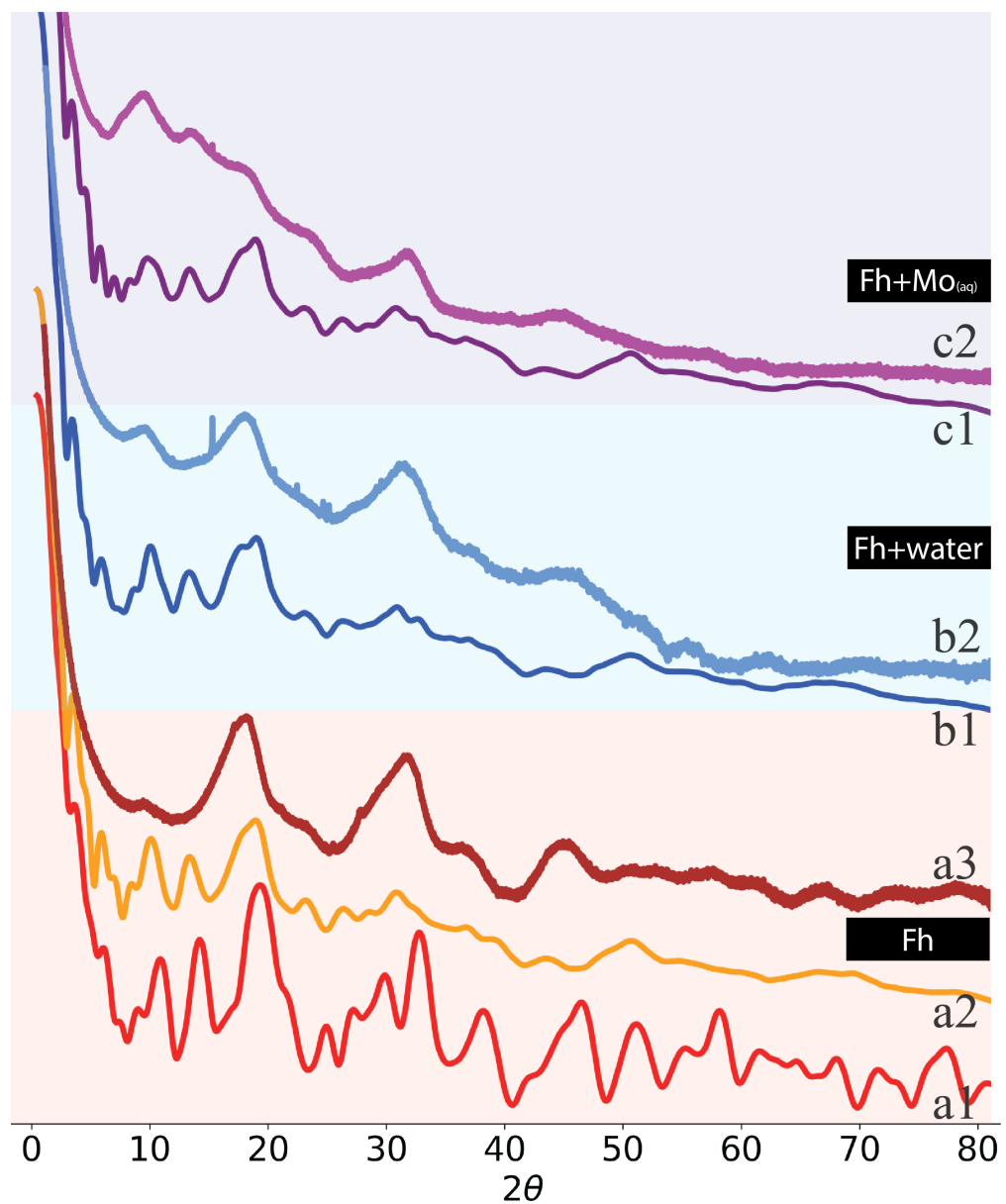


Figure 1: Comparative XRD analysis of Fh: structural insights from simulated and synthesized environments with $[Mo]_{aq}$. XRD pattern for a1) Michel's crystallographic structure of Fh , a2) MD-relaxed Fh slab, a3) synthesized Fh , b1) Fh slab and water (Mo-0) , b2) synthesized Fh and water , c1) Fh slab with $[Mo]_{aq}$ (Mo-8), and c2) synthesized Fh with $[Mo]_{aq}$.

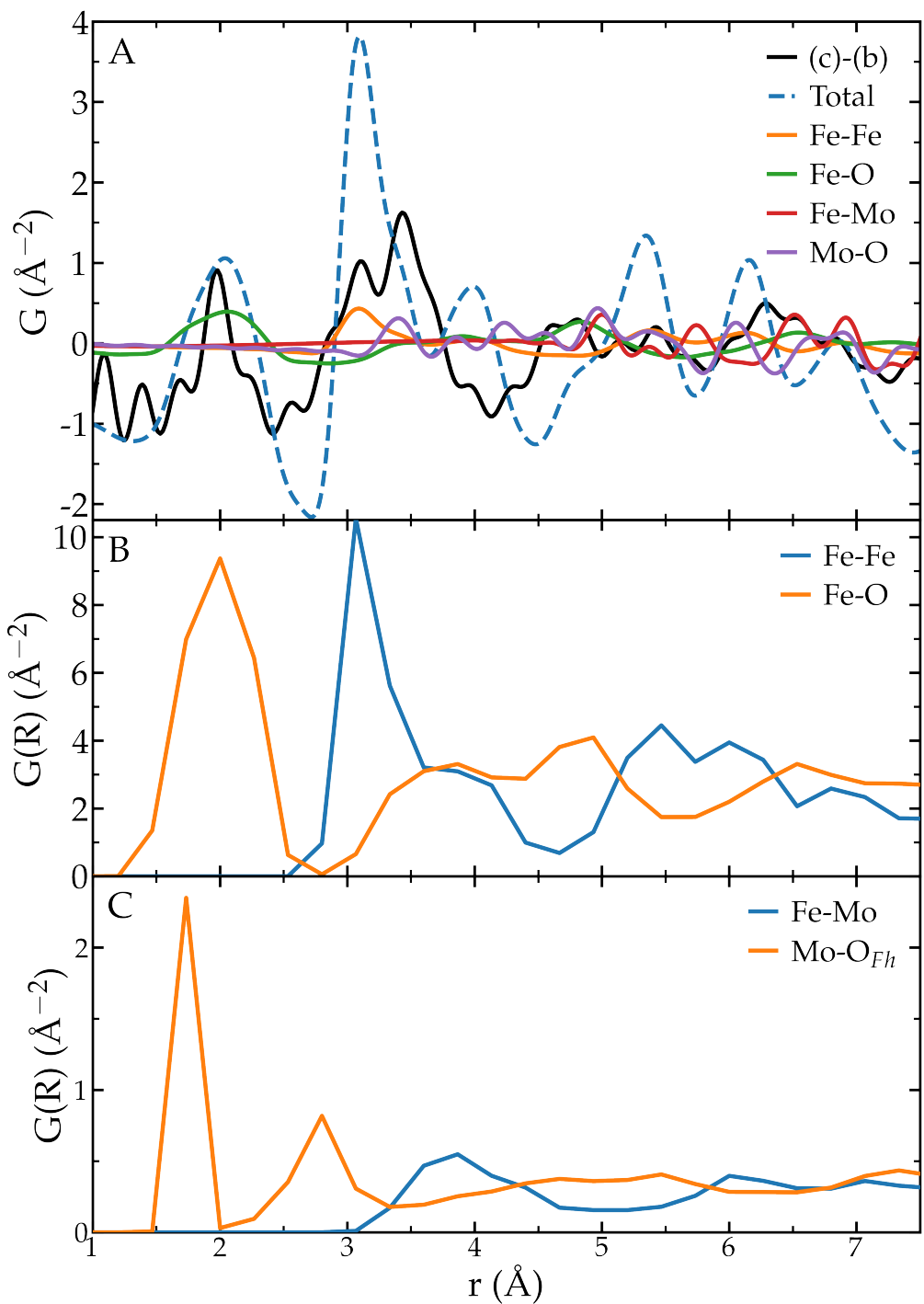


Figure 2: Pair-wise distances at the Fh-water interface: insights from d-PDF and RDF analyses with adsorbed $[\text{Mo}]_{\text{aq}}$. A) d-PDF plot resulted from the subtraction of Fh/water (b) PDF from Fh/water/[Mo]_{aq} (c) PDF ((c)-(b)) along with simulated PDF plots from Mo-9 representing the total calculated PDF (total), and contributions from different scattering pairs Fe–Fe (scaled by 0.1), Fe–O (scaled by 0.2), Fe–Mo (scaled by 50), and Mo–O (scaled by 100). B) Calculated RDF plots of Fh in the presence of [Mo]_{ads} for Fe–Fe and Fe–O pairs. C) Calculated RDF plots of [Mo]_{aq} with Fh Fe (Fe–Mo) and O (Mo–O_{Fh}) atoms.

223 adsorbed Mo ($[Mo]_{ads}$), provides a bottom-up approach for interpreting the measured PDF.
224 This simulated total PDF aligns with the d-PDF at peak positions, exhibiting peaks at 2.04
225 Å and a broad peak with a shoulder at 3.10 Å. Detailed analysis of individual scattering pairs
226 reveals that the simulated PDF comprises peaks at 2.06 Å for Fe–O, while the broad feature
227 is a composite of Fe–Fe and Mo–O contributions at 3.09 Å and 3.40 Å, respectively. The
228 absence of the first shell peak for Mo–O in $[MoO_4]^{2-}_{aq}$ is attributed to its low abundance.

229 Analysis of the RDF from MD trajectories (Figure 2-B), effectively determines pairwise
230 distances during simulations. The reactive MD approach, by successfully reproducing the
231 Fh structure in contact with water and at varying $[Mo]_{aq}$ concentrations, demonstrates the
232 appropriateness of the chosen force field. This is further substantiated by both the measured
233 PDF and RDF, which confirm that the Fh bulk maintains its local structure throughout the
234 simulations aligning with reported values of 1.98 and 3.04 Å for Fe–Fe and Fe–O distances,
235 respectively⁶⁹.

236 RDF analysis additionally enables the monitoring of prevalent $[Mo]_{aq}$ distances to the Fh
237 surface (Figure 2-C). Notably, the peak positions remaining unaffected across different $[Mo]_{aq}$
238 concentrations suggests the energetically favorable nature of $[Mo]_{aq}$ interactions with the
239 surface. The first shell peak at 1.73 Å, indicative of inner-sphere, octahedrally-coordinated
240 Mo–O, aligns with values from extended X-ray absorption fine structure (EXAFS) (1.77
241 Å)⁷¹ and X-ray scattering (1.78 Å)⁷². This distance is comparable with the Mo–O bond
242 length in hematite (1.73 Å)¹⁹, and to As–O (1.68 Å) on Fh⁷³. The model architecture allows
243 for exchange processes that extend beyond proton transfer reactions and allows the formation
244 of directly-bound $[Mo]_{aq}$ complexes which are a result of the exchange of oxygen atoms. RDF
245 analysis also facilitates the observation of adsorbed, fully water-solvated $[Mo]_{aq}$ species. The
246 second shell peak at 2.80 Å corresponds to outer-sphere adsorbed $[Mo]_{aq}$ complexes. The
247 broad Mo–Fe feature (3.2-4.5 Å) encompasses both inner- and outer-sphere adsorbed $[Mo]_{aq}$
248 complexes, aligning with the EXAFS reported range of 3.28-3.53 Å for Fh Mo–Fe⁷⁴. Notably,
249 the proximity of outer-sphere complexes to inner-sphere complexes at these distances suggests

250 the potential for exchange between these states depending on the concentration of $[Mo]_{aq}$
251 (*vide infra*).

252 Surface Interactions and Structural Dynamics

253 At equilibrium, the calculated surface charge of the Fh slab reveals a net positively charged
254 top and bottom layer. This positive charge primarily results from Fe atoms and surface
255 protons at pH = 7. This observation aligns with the reported point of zero charge (PZC) for
256 Fh (PZC=7-9)⁷⁵.

257 To investigate the impact of $[Mo]_{aq}$ adsorption on Fh charge distribution, a charge differ-
258 ence plot was generated, comparing Fh in vacuum to Fh/water/ $[Mo]_{aq}$ (Mo-8) (Figure 3-A).
259 This plot reveals localized sites, where the adsorption of negatively charged $[Mo]_{aq}$ leads to
260 short-range, localized charge perturbations. These perturbations are specifically confined to
261 regions where $[Mo]_{aq}$ forms inner-sphere complexes with the surface (Figure SI 6). Following
262 charge equilibration, these localized charge transfers collectively lead to a change in the total
263 surface charge of Fh.

264 The charge probability distribution for Fh (Figure 3-B) displays distinct characteris-
265 tics, with positively-charged Fe and H atoms, alongside negatively-charged oxygen atoms.
266 Notably, the O atom charge distribution exhibits a doublet-like feature. Upon detailed anal-
267 ysis, the more negative peak is attributed to surface oxygens, while the relatively positive
268 one corresponds to bulk Fh oxygen atoms, in water. The ITIM algorithm analysis, both in
269 the presence (Mo-8) and absence (Mo-0) of $[Mo]_{aq}$, reveals that the more negatively-charged
270 oxygens are located at the interfacial regions on the top or bottom of the Fh slab (Figures
271 SI 7 and SI 8). In the case of Mo-8, the adsorption of negatively-charged $[Mo]_{aq}$ shifts the
272 charge distribution of Fh oxygen atoms towards a more pronounced interfacial character,
273 further indicating a charge transfer to the surface.

274 Calculating the surface charge as a function of $[Mo]_{aq}$ concentration (Figure 3-C) indicates
275 that water alone minimally alters the relative surface charge of Fh. As the concentration of

[Mo]_{aq} increases, the surface charge of Fh becomes more negative. However, at higher [Mo]_{aq} concentrations, the relative surface charge does not continue to decrease but instead reaches a plateau, as observed in the Mo-6 and Mo-8 regimes. This plateau phase is characterized by larger error margins in surface charge, particularly in Mo-8, indicative of non-classical overcharging behavior. This behavior is influenced by pronounced ion-ion association, which affect the structure of the interfacial water hydrogen bond network, competition for adsorption sites on Fh, and the polymerization equilibria of [Mo]_{aq} species⁷⁶.

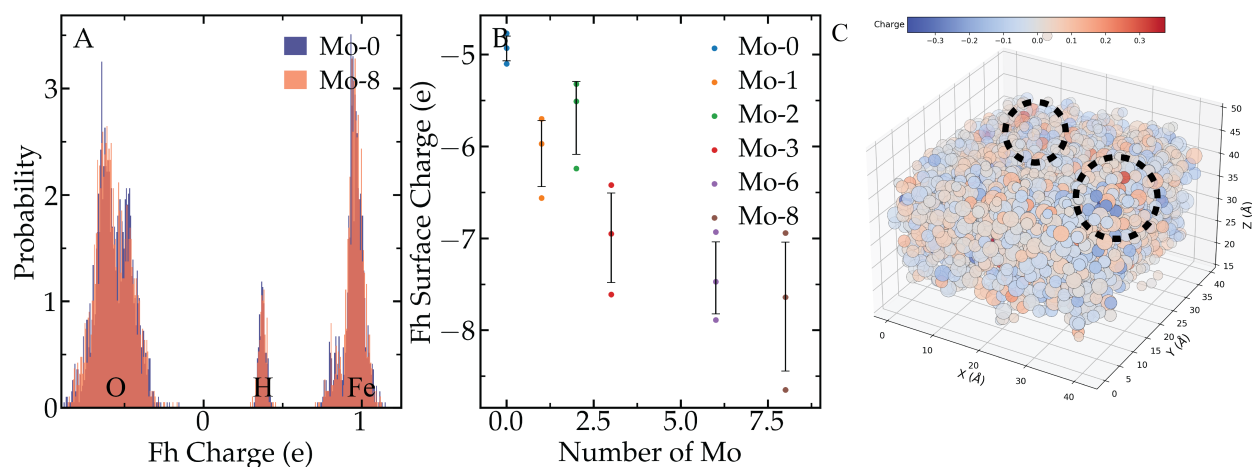


Figure 3: Surface charge analysis of Fh: impacts of [Mo]_{aq} adsorption on surface charge distribution. A) Charge probability distribution of Fh in Mo-0 and Mo-8. B) Calculated surface charge as a function of the number of [Mo]_{aq}. C) Calculated equilibrium atomic charge difference between Mo-0 and Mo-8. Circled areas show the spots with the highest charge perturbations.

The structural dynamics of Fh during simulations are further elucidated by analyzing the Fe–O–Fe bond angle probability distribution (Figure SI 9). The initial nano-crystalline Michel Fh structure⁷⁰ comprises both tetrahedral (109.5°) and octahedral (90° , 180°) Fe atoms. During MD relaxation and upon contact with water, the sharp features of angle probability distribution broaden, yet the tetrahedral-octahedral coordination environment of Fe is retained. This observation aligns with calculations suggesting that at 298 K, for a simulated Fh with a diameter of ~ 3 nm, the Michel model remains slightly more stable⁷⁷. In our simulations, the initial Michel's Fh structure does not undergo a phase transformation into a fully octahedral Fe structure, also referred to as the Manceau Fh model. This high-

²⁹² lights the stability and persistence of the mixed coordination environment under simulated
²⁹³ conditions.

²⁹⁴ The presence of $[Mo]_{aq}$, at both low and high concentrations simulated (Mo-3 and Mo-
²⁹⁵ 8), does not appear to induce any noticeable changes in the Fe–O–Fe angle distribution
²⁹⁶ (Figure SI 10). This observation highlights the interfacial nature of $[Mo]_{aq}$ interactions with
²⁹⁷ Fh, suggesting that the $[Mo]_{aq}$ primarily affects the surface rather than altering the bulk
²⁹⁸ structure of Fh.

²⁹⁹ The Chemistry of Water at Ferrihydrite Interface and Solution

³⁰⁰ We also explored non-covalent interactions, especially the HB network of water at the Fh-
³⁰¹ water interface. These interactions influence the structure and dynamics at the solid-water
³⁰² interface⁷⁸, impacting geochemical processes such as crystallization⁷⁹ and isotopic fractiona-
³⁰³ tion⁸⁰. In contrast to classical MD, where hydrogen bonds are not predefined and are instead
³⁰⁴ determined based on energy and geometric criteria⁸¹, the ReaxFF force field declares hy-
³⁰⁵ drogen bonding a priori in our reactive simulations. This approach enables more realistic
³⁰⁶ simulations, particularly effective in predicting the short-range cohesive forces within wa-
³⁰⁷ ter.⁸².

³⁰⁸ The average number of HBs ($\langle N_H \rangle$) (Figure 4-A) gradually increases with distance from
³⁰⁹ the Fh surface. This trend results from the restricted mobility and fewer accessible config-
³¹⁰ urations of water molecules at the interface, leading to a reduced number of HBs compared
³¹¹ to bulk water⁸³. For the Fh/water system (Mo-0), $\langle N_H \rangle$ approaches that of bulk water at
³¹² approximately 6 Å from the surface, with a transition region extending from about ~2.5 to
³¹³ 6 Å. In the presence of $[Mo]_{aq}$ (Mo-8), this interfacial-to-bulk HB transition region extends
³¹⁴ slightly further from the surface, before HB dynamics returns to its unperturbed bulk wa-
³¹⁵ ter state. This effect is most pronounced in the 2-5 Å region from the surface, correlating
³¹⁶ with the coexistence of inner- and outer-sphere $[Mo]_{aq}$ complexes, which can act as both HB
³¹⁷ donors and acceptors.

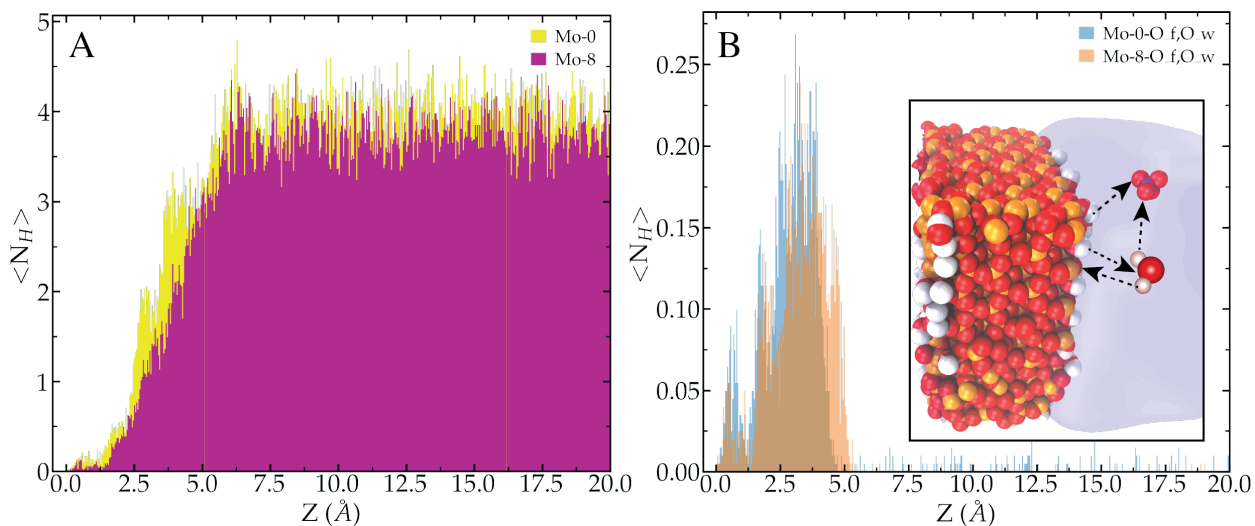


Figure 4: Effect of $[Mo]_{aq}$ on the HB network at the interface of Fh-water: Average number of hydrogen bonds as a function of distance from the surface, A) for Fh for Mo-0, and Mo-8. B) for surface oxygen O_f donors and water oxygen O_w acceptors. Inset) shows surface, water, and MoO_4^{2-} can act as HB donors and acceptors. For the latter, the simulations show the formation of protonated $\text{MoO}_{4\text{aq}}^{2-}$ species that can act as HB donors (not shown in this image).

[Mo]_{aq} influences the hydrogen HB donor abilities of both surface and water oxygens (O_f and O_w), with its impact being more pronounced on water oxygens (O_w) in forming HBs with Fh surface oxygens (Figure SI 11). In the presence of [Mo]_{aq} (Mo-8), the O_w donor population shifts away from the surface, compared to the Fh/water system (Mo-0). This shift leads to a decrease in the average number of HBs involving O_w donors ($O_w \cdots O_f$), a consequence of the competitive adsorptive interactions between [Mo]_{aq} and Fh, limiting water's access to the surface. Regarding Fh surface donors (O_f) ((Figure 4)-B), the presence of [Mo]_{aq} in Mo-8 extends the range within which the surface can act as a donor. [Mo]_{aq} effectively out-competes water as an HB acceptor up to 5 Å from the surface, shaping a new HB network with water.

For the HB acceptor abilities of $\text{MoO}_{4(aq)}^{2-}$ oxygen atoms (O_m) (Figures SI 12 and SI 13), at distances greater than 5 Å, [Mo]_{aq} is fully solvated and primarily accepts HBs from water. As the concentration of [Mo]_{aq} increases from Mo-3 to Mo-8, a broader range of HB interactions between $O_f \cdots O_m$ emerges, indicating the onset of [Mo]_{aq} adsorption.

³³² [Mo]_{aq} HB donor abilities (Figure SI 14), suggest that the reactive simulation predicts the
³³³ formation of protonated [Mo]_{aq} species with lifetimes long enough to form HBs. Adsorbed
³³⁴ [Mo]_{aq} out-competes water in HB donor abilities up to 5 Å from the surface.

³³⁵ The HB acceptor and donor abilities of O_m emphasize the crucial role of outer-sphere
³³⁶ complexes in mediating surface interactions through HBs⁸⁴. The disruption of HB networks is
³³⁷ energetically costly, and the surface HB abilities determine its affinity to water. Additionally,
³³⁸ interfacial HB between solutes and water likely reduce its adsorption energy⁸⁵. Consequently,
³³⁹ the model predicts various pathways that affect the adsorption free energy.

³⁴⁰ The reactive simulations provide insights into the behavior of species in bulk solution,
³⁴¹ particularly highlighting the exchange of oxygen atoms between water and molybdate groups
³⁴² (Figure SI 15). This exchange is evident when monitoring the distance of Mo with water
³⁴³ oxygens within a 4 Å shell. Over time, and as hydration of [Mo]_{aq} progresses, water oxygens
³⁴⁴ segregate into two distinct groups around [Mo]_{aq}: directly bonded oxygens at ~1.78 Å,
³⁴⁵ forming Mo=O_w bonds, consistent with the reported experimental value⁷², and the first
³⁴⁶ hydration shell observed at 2-2.5 Å. This is also reflected in RDF of Mo and water oxygen
³⁴⁷ (Mo–O_w) (Figure SI 16). The results suggest that at equilibrium in solution, Mo–O_m bonds
³⁴⁸ are susceptible to hydrolysis, indicating the dynamic and reactive nature of the hydration
³⁴⁹ process.

³⁵⁰ Furthermore, the model accurately describes the behavior of solvents and counter-ions.
³⁵¹ The RDF of water (O_w–O_w) (Figures SI 17) gives a good reproduction of both experimental
³⁵² and ReaxFF values at room temperature⁸⁶. Notably, there is a slight increase in the height
³⁵³ of the first peak of the water O_w–O_w RDF. This difference may be attributed to stronger
³⁵⁴ interactions between water molecules, potentially heightened by nano-confinement effects
³⁵⁵ between hydrophilic Fh layers⁸⁶. In addition, the RDF of Na–O_w (Figure SI 18), suggests
³⁵⁶ a hydrated Na⁺ cation with a water solvation shell at 2.50 Å. This observation aligns with
³⁵⁷ the reported values for ReaxFF electrolyte systems⁵², further validating the model accuracy
³⁵⁸ in describing the solvation structure of Na⁺ in aqueous environments.

359 **Bridging Reactive Molecular Dynamics With Surface Com-**
360 **plexation Models**

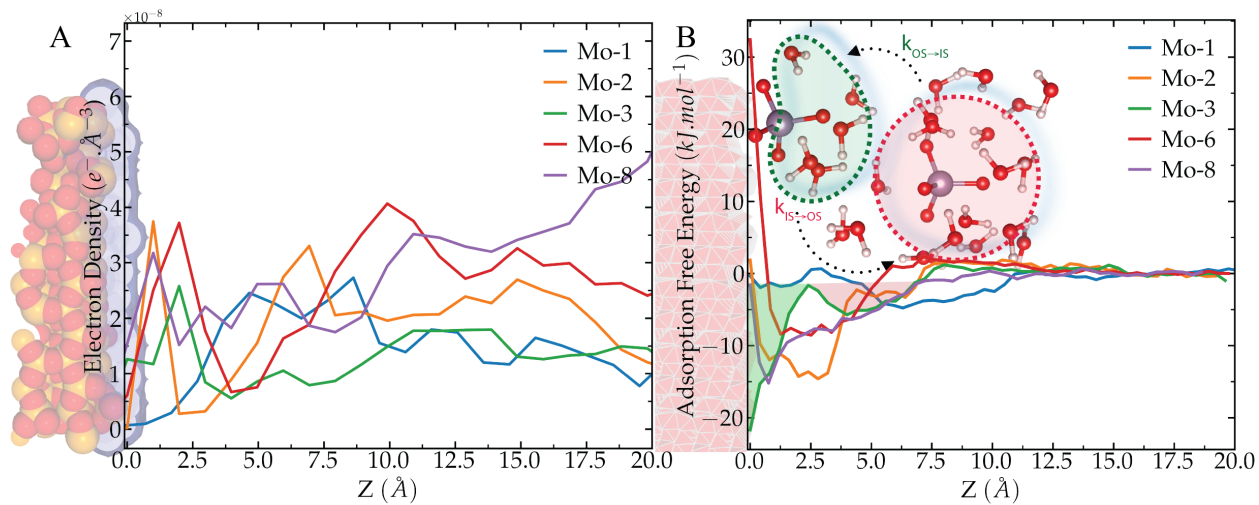


Figure 5: Free energy landscape of $[\text{Mo}]_{\text{aq}}$ adsorption at the ferrihydrite-water interface A) Electron density profile of $[\text{Mo}]_{\text{aq}}$ from the surface of Fh. The surface is defined by the uppermost layer of Fh depicted with the blue region at zero. B) Free energy of adsorption of $[\text{Mo}]_{\text{aq}}$ as a function of distance from the surface of Fh. Green and red shaded areas show the regions where inner- and outer-sphere adsorbed complexes exist. The arrows denote the exchange between the two complexes.

361 **Energetics of Adsorption**

362 The electron density profiles of $[\text{Mo}]_{\text{aq}}$ as a function of distance from the Fh surface (Figure
363 5-A) offer a kinetic perspective on $[\text{Mo}]_{\text{aq}}$ distribution. This surface is defined as the top
364 interfacial layer of Fh, identified using the ITIM algorithm in each simulation snapshot. The
365 dynamic and rough nature of the Fh surface necessitates this approach.

366 At infinite dilution (Mo-1), the non-zero electron density at a range of distances of 2.5-10
367 Å from the surface and farther in the bulk solution, indicates that $[\text{Mo}]_{\text{aq}}$ moves between the
368 adsorbed and diffused states. As the concentration of $[\text{Mo}]_{\text{aq}}$ increases from Mo-2 to Mo-8,
369 the inner-sphere complexes move closer to the surface at a distance of 2-4 Å, and outer-sphere
370 complexes are positioned in 4-7 Å from the surface. At higher concentrations (Mo-6, Mo-8),

more $[Mo]_{aq}$ are also present at farther distances to up to 10-15 Å and rather than in the bulk solution signifying the strength of adsorptive interactions between $[Mo]_{aq}$ and Fh. At lower concentrations (Mo-2, Mo-3), the electron density peaks corresponding to inner- and outer-sphere complexes of $[Mo]_{aq}$ show minimal or no overlap, suggesting less exchange of $[Mo]_{aq}$ between these two adsorbed states. However, at higher concentrations (Mo-6, Mo-8), there is a notable overlap between the peaks for inner- and outer-sphere complexes. This overlap indicates a facilitated exchange between the two states.

As previously discussed in the Methods section, to comprehensively access the full range of the free energy landscape and the probability distribution of $[Mo]_{aq}$ as a function of distance from the surface (Figure 5-B) (SI 21), umbrella sampling is employed. This technique is capable of sampling states that are high in energy, with energy barriers exceeding $k_B T$ (2.479 kJ.mol⁻¹ at 298 K), which are often referred to as rare events.

At infinite dilution (Mo-1) the free energy shows a flat profile with small energy barriers between different adsorbed states and bulk states, consistent with the electron density profile. At relatively low concentrations of $[Mo]_{aq}$ (Mo-2-3), two distinct adsorbed states of – inner- and outer-sphere complexes – are predominantly observed. Inner-sphere complexes, forming at distances of up to 3 Å from the surface, are more energetically favorable by about 15-20 kJ.mol⁻¹ compared to outer-sphere complexes at distances >3-7.5 Å. This energy difference results in a lower desorption rate ($k_{IS \rightarrow OS}$) from the surface consistent with electron density profiles for Mo-3 mostly consisting of inner-sphere complexes and Mo-2 having two distinct absences of electron density at the onset of ~2.5 Å. Meanwhile, outer-sphere complexes are located at 4-5 Å from the surface, characterized by a smaller or negligible energy barrier and a higher rate of transition to inner-sphere complexes ($k_{OS \rightarrow IS}$). The observed energy barrier between the inner- and outer-sphere states in both directions is likely attributable to the solvation/desolvation of $[Mo]_{aq}$, the displacement and reorientation of water in the solvation sphere of $[Mo]_{aq}$ and at the Fh surface, and the disruption of the hydrogen bond network at the interface⁸⁷.

398 At higher $[Mo]_{aq}$ concentrations (Mo-6 to Mo-8), the adsorption free energy ranges be-
399 tween -15 and -10 kJ.mol⁻¹. In this regime, the energy barrier between inner- and outer-
400 sphere complexes disappears entirely. This phenomenon is likely due to the effects of surface
401 charge screening by the adsorbed $[Mo]_{aq}$ species^{88,89}.

402 Acidity of Surface Protons

403 We have selected Fh surface protons based on their equilibrium charge (high, low, medium)
404 (Figure SI 22) after reactive MD in water (Mo-0) to calculate the pK_a of the corresponding
405 surface oxygen sites using umbrella sampling. Surface acidity, determined by the pK_a of
406 surface hydroxyl groups is foundational in predictive SCM. These pK_a 's which are generally
407 found by titration measurements are not capable of assigning individual pK_a 's for different
408 surface protons and are challenging due to mineral dissolution during the titration. The sur-
409 face reactivity strongly depends on the surface acidity and is critical in understanding the
410 adsorption of solutes at water-mineral interfaces. Computational approaches to calculating
411 unique surface species pK_a do not rely on fitting experimental parameters and can yield val-
412 uable information on surface chemical behavior and its interface with water. The idea behind
413 these computational methods is to calculate the free energy difference between the proto-
414 nated/deprotonated surface sites mostly through *ab initio* MD, and PMF techniques^{90,91}.
415 The studied deprotonation sites are selected based on their chemical environment (coordi-
416 nation number -connected to 1 or 2 Fe or species Al-OH vs Si-OH).

417 The summarized results (Table 1) show surface deprotonation is an endergonic process
418 in water at pH = 7. The results also show that there is no direct relationship between the
419 initial charge of the proton and its pK_a value giving an emphasis to other factors, such as the
420 local chemical environment of the proton, its interface, (de)hydration effects, and hydrogen
421 bonding affecting the final deprotonated state of the hydrogen atoms. The calculated pK_a
422 values agree well with reported charge distribution multi-site ion complexation (MUSIC)
423 model calculations for (1̄10) surface of Fh with $pK_a = 7.17$ slightly underestimated while

Table 1: Fh surface acidity calculations: umbrella sampling results versus MUSIC models. Computed surface deprotonation free energies ΔG and pK_a values of surface protons, compared with results from MUSIC model

Proton (ReaxFF Charge)	ΔG (kJ.mol ⁻¹)	pK_a	MUSIC Model ^a	
			Species	pK_a
1 (Medium)	48.1 ± 0.6	8.40 ± 0.1	Fe ₂ OH	8.2
2 (High)	40.9 ± 0.4	7.17 ± 0.07	FeOH ₂	8.0
3 (Low)	33.4 ± 0.4	5.85 ± 0.08	Fe ₃ OH	5.5

^a From reference⁴⁶.

424 being within 1 pK_a unit.

425 Adsorption Constants

426 The adsorption constants for different $[Mo]_{aq}$ complexes with the surface of Fh, calculated
427 by SCM, linear free energy relationships (LFER) and the current study are summarized in
428 Table 2. Although the SCM calculations for adsorbed inner-sphere complexes are performed
429 at pH > 5 and with taking into account the acidity of $(HO)MoO_3^-$ ($pK_a=4.2$), partially or
430 fully protonated Mo species needed to be introduced to improve the model. The calculated
431 adsorption constant for MoO_4^{2-} adsorbed as $FeOHMoO_4^{-2}$, from reactive simulations free
432 energy profile, was found to be 3.14, slightly higher than the value by LFER calculation.
433 Using the adsorption PMF results (Figure 5-B), the adsorption constants for $[Mo]_{aq}$ in Mo-
434 1-8 were calculated. The weight-averaged $LogK_a$ over all trajectories was then calculated
435 using the Equations 3-4. The calculated $LogK_a$ of 3.39 is attributable to the greater influ-
436 ence (lower error) of data points in regimes of higher concentration, potentially due to a
437 better representation of experimental conditions. The observed slight difference with SCM
438 fitting methodologies can be linked to the use of different parameters in deriving the values.
439 However, the general agreement with the reported values suggests a holistic approach that
440 can be further expanded by varying simulation conditions.

Table 2: Concentration-dependent adsorption constants of $[Mo]_{aq}$ onto Fh: insights from reactive MD and comparisons with SCM models. Calculated adsorption equilibrium constant (uncertainty) LogK_a (σ) of $[Mo]_{aq}$ on the surface of Fh from free energies of adsorption derived from umbrella sampling PMFs and reported values from SCM and LFER

Species	LogK_a	(σ)
Fh-[Mo] _{aq} Mo-1	0.864	0.001
Fh-[Mo] _{aq} Mo-2	2.543	0.006
Fh-[Mo] _{aq} Mo-3	3.785	0.0001
Fh-[Mo] _{aq} Mo-6	1.500	0.001
Fh-[Mo] _{aq} Mo-8	2.664	0.0009
Weighted Average	3.169	0.0002
^a FeOHMoO_4^{2-}	3.14	0.039
^b FeOHMoO_4^{2-}	2.4	

^a From SCM²³.

^b From LFER⁹².

441 Environmental Implications

442 Global biogeochemical N, C, and S cycles that have shaped the environmental and biological
 443 co-evolution of Earth are dependent upon the mobility and the bioavailability of aqueous nu-
 444 trient and contaminant elements, such as oxidoreductase enzymes cofactors requiring cellular
 445 uptake of aqueous molybdate (MoO_4^{2-}) ions^{42,43}.

446 Geochemical reactions involving Fe- and S-bearing minerals have regulated MoO_4^{2-} mo-
 447 bility and availability over geologic time^{1,2}. Interfacial reactions with Fe(III) (oxyhydr)oxide
 448 (FeO_x) phases often limit aqueous MoO_4^{2-} concentrations in soils, sediments, and waters^{4,5}.

449 Unravelling these complex reaction mechanisms and pathways is important for understand-
 450 ing MoO_4^{2-} availability in modern environments and paleoenvironments. SCM commonly
 451 used to describe the adsorption of nutrient and pollutant elements rely on assumptions that
 452 can be furthered refined to provide new insights into these interfacial interactions. Here, we
 453 employ reactive MD and synchrotron X-ray techniques to show how hydration and adsorp-
 454 tion of aqueous MoO_4^{2-} affects the surface charge of Fh which initiates a restructuration
 455 towards a more disordered phase response observable in simulations and experiments. The
 456 Fh surface charge change due to interfacial interactions is concentration-dependent and af-

457 fects a wide range of chemistry at the interface such as hydrogen bonding and even the
458 dynamics and energetics of exchange between inner- and outer-sphere adsorbed complexes
459 with important implications for the bioavailability and transport of the aqueous species, as
460 well as, implications in isotopic fractionation mechanisms⁹³. The accuracy of our model was
461 further tested by deriving SCM parameters for Fh surface acidity and the adsorption con-
462 stants of $[Mo]_{aq}$ showing excellent agreement with the literature. This new approach enables
463 informing and improving SCM where experimental work is not feasible or for expanding the
464 chemical conditions explored for accurately describing adsorption via SCM or our current
465 model. This work offers a new way of looking into interfacial processes and more studies
466 about phase transformation of other Fe (oxy)hydroxide phases with different aqueous metals
467 is currently underway.

468 Acknowledgement

469 A. H. thank Miles A. Shumaker and C. J. Fennell for providing guidance and direction.
470 AH also thank NSERC-CREATE to INSPIRE for the fellowship (Grant No. CREATE-
471 555378-2021). Funding was provided by the Natural Sciences and Engineering Research
472 Council of Canada (NSERC) through a Discovery Grant (Grant No. RGPIN-2020-05172)
473 held by MBJL. The computational aspects of this research were enabled in part by support
474 provided by University of Saskatchewan research computing (Plato) and the Digital Research
475 Alliance of Canada. Part or all of the research described in this paper was performed at
476 the Canadian Light Source, a national research facility of the University of Saskatchewan,
477 which is supported by the Canada Foundation for Innovation (CFI), the Natural Sciences
478 and Engineering Research Council (NSERC), the National Research Council (NRC), the
479 Canadian Institutes of Health Research (CIHR), the Government of Saskatchewan, and the
480 University of Saskatchewan. S. G. acknowledges fundings from the European Union's Horizon
481 2020 research and innovation programme under the Marie Skłodowska-Curie grant agreement

⁴⁸² No 101065060.

⁴⁸³ Author Information

⁴⁸⁴ Corresponding Authors

⁴⁸⁵ **Ardalan Hayatifar** - Department of Geological Sciences, University of Saskatchewan,

⁴⁸⁶ Saskatoon, SK, Canada S7N 5E2; <https://orcid.org/0000-0002-7884-6917>;

⁴⁸⁷ Email: ardalan.hayatifar@usask.ca

⁴⁸⁸ **Matthew B.J. Lindsay** - of Geological Sciences, University of Saskatchewan, Saskatoon,

⁴⁸⁹ SK, Canada S7N 5E2; <https://orcid.org/0000-0001-9123-3261>;

⁴⁹⁰ Email: matt.lindsay@usask.ca

⁴⁹¹ Authors

⁴⁹² **Simon Gravelle** - University Grenoble Alpes, CNRS, LIPhy, 38000 Grenoble, France;

⁴⁹³ <https://orcid.org/0000-0003-2149-6706>;

⁴⁹⁴ Email: simon.gravelle@cnrs.fr

⁴⁹⁵ **Beatriz D. Moreno** - Brockhouse Diffraction Sector, Canadian Light Source, Saskatoon,

⁴⁹⁶ SK, Canada; Email: Beatriz.diazmoreno@lightsource.ca

⁴⁹⁷ **Valerie A. Schoepfer** - Department of Geological Sciences, University of Saskatchewan,

⁴⁹⁸ Saskatoon, SK, Canada S7N 5E2; <https://orcid.org/0000-0002-9582-9940>;

⁴⁹⁹ Email: valerie.schoepfer@usask.ca

⁵⁰⁰ Competing Interests

⁵⁰¹ The authors declare no competing interests.

502 **Supporting Information Available**

503 The following files are available free of charge.

- 504 • Supporting Information

505 **References**

- 506 (1) Scott, C.; Lyons, T. W. Contrasting molybdenum cycling and isotopic properties in
507 euxinic versus non-euxinic sediments and sedimentary rocks: Refining the paleoproxies.
508 *Chemical Geology* **2012**, *324–325*, 19–27.
- 509 (2) Parnell, J.; Spinks, S.; Andrews, S.; Thayalan, W.; Bowden, S. High Molybdenum
510 availability for evolution in a Mesoproterozoic lacustrine environment. *Nature Commu-*
511 *nicaions* **2015**, *6*.
- 512 (3) Pichler, T.; Koopmann, S. Should Monitoring of Molybdenum (Mo) in Groundwater,
513 Drinking Water and Well Permitting Made Mandatory? *Environmental Science &*
514 *Technology* **2019**, *54*, 1–2.
- 515 (4) Ge, X. et al. Iron- and aluminium-induced depletion of molybdenum in acidic environ-
516 ments impedes the nitrogen cycle. *Environmental Microbiology* **2018**, *21*, 152–163.
- 517 (5) Yang, P.-T.; Wang, S.-L. Sorption and speciation of molybdate in soils: Implications
518 for molybdenum mobility and availability. *Journal of Hazardous Materials* **2021**, *408*,
519 124934.
- 520 (6) Wang, X.; Li, W.; Harrington, R.; Liu, F.; Parise, J. B.; Feng, X.; Sparks, D. L. Effect
521 of Ferrihydrite Crystallite Size on Phosphate Adsorption Reactivity. *Environmental*
522 *Science & Technology* **2013**, *47*, 10322–10331.
- 523 (7) Boily, J.-F.; Song, X. Direct identification of reaction sites on ferrihydrite. *Communi-*
524 *cations Chemistry* **2020**, *3*.

- 525 (8) Gonella, G.; Backus, E. H. G.; Nagata, Y.; Bonthuis, D. J.; Loche, P.; Schlaich, A.;
526 Netz, R. R.; Kühnle, A.; McCrum, I. T.; Koper, M. T. M.; Wolf, M.; Winter, B.;
527 Meijer, G.; Campen, R. K.; Bonn, M. Water at charged interfaces. *Nature Reviews
528 Chemistry* **2021**, *5*, 466–485.
- 529 (9) Fukushi, K.; Sato, T. Using a Surface Complexation Model To Predict the Nature and
530 Stability of Nanoparticles. *Environmental Science & Technology* **2005**, *39*, 1250–1256.
- 531 (10) Majzlan, J. Thermodynamic Stabilization of Hydrous Ferric Oxide by Adsorption of
532 Phosphate and Arsenate. *Environmental Science & Technology* **2011**, *45*, 4726–4732.
- 533 (11) Namayandeh, A.; Borkiewicz, O. J.; Bompotis, N. M.; Chrysochoou, M.; Michel, F. M.
534 Oxyanion Surface Complexes Control the Kinetics and Pathway of Ferrihydrite Trans-
535 formation to Goethite and Hematite. *Environmental Science & Technology* **2022**, *56*,
536 15672–15684.
- 537 (12) Björneholm, O.; Hansen, M. H.; Hodgson, A.; Liu, L.-M.; Limmer, D. T.;
538 Michaelides, A.; Pedevilla, P.; Rossmeisl, J.; Shen, H.; Tocci, G.; Tyrode, E.; Walz, M.-
539 M.; Werner, J.; Bluhm, H. Water at Interfaces. *Chemical Reviews* **2016**, *116*, 7698–
540 7726.
- 541 (13) Ruiz-Lopez, M. F.; Francisco, J. S.; Martins-Costa, M. T. C.; Anglada, J. M. Molecular
542 reactions at aqueous interfaces. *Nature Reviews Chemistry* **2020**, *4*, 459–475.
- 543 (14) Schoepfer, V. A.; Lindsay, M. B. Repartitioning of co-precipitated Mo(VI) during Fe(II)
544 and S(-II) driven ferrihydrite transformation. *Chemical Geology* **2022**, *610*, 121075.
- 545 (15) Botella, R.; Lefèvre, G. A deep look into the diverse surface speciation of the mono-
546 molybdate/lepidocrocite system by ATR-IR and polarized ATR-IR spectroscopy. *Col-
547 loids and Surfaces A: Physicochemical and Engineering Aspects* **2022**, *647*, 129065.

- 548 (16) Schoepfer, V. A.; Lum, J. E.; Lindsay, M. B. J. Molybdenum(VI) Sequestration Mech-
549 anisms During Iron(II)-Induced Ferrihydrite Transformation. *ACS Earth and Space*
550 *Chemistry* **2021**, *5*, 2094–2104.
- 551 (17) Görn, M. G.; Bolanz, R. M.; Parry, S.; Göttlicher, J.; Steininger, R.; Majzlan, J.
552 INCORPORATION OF Mo₆⁺ IN FERRIHYDRITE, GOETHITE, AND HEMATITE.
553 *Clays and Clay Minerals* **2021**, *69*, 188–204.
- 554 (18) Das, S.; Essilfie-Dughan, J.; Jim Hendry, M. Sequestration of molybdate during trans-
555 formation of 2-line ferrihydrite under alkaline conditions. *Applied Geochemistry* **2016**,
556 *73*, 70–80.
- 557 (19) Zhang, J.; Coker, V. S.; Mosselmans, J. F. W.; Shaw, S. Adsorption of octahedral mono-
558 molybdate and poly-molybdate onto hematite: A multi-technique approach. *Journal of*
559 *Hazardous Materials* **2022**, *431*, 128564.
- 560 (20) Goldberg, S. *Advances in Agronomy Volume 47*; Elsevier, 1992; pp 233–329.
- 561 (21) Satpathy, A.; Wang, Q.; Giamar, D. E.; Wang, Z. Intercomparison and Refinement of
562 Surface Complexation Models for U(VI) Adsorption onto Goethite Based on a Metadata
563 Analysis. *Environmental Science & Technology* **2021**, *55*, 9352–9361.
- 564 (22) Gustafsson, J. P.; Tiberg, C. Molybdenum binding to soil constituents in acid soils: An
565 XAS and modelling study. *Chemical Geology* **2015**, *417*, 279–288.
- 566 (23) Gustafsson, J. P. Modelling molybdate and tungstate adsorption to ferrihydrite. *Chem-
567 ical Geology* **2003**, *200*, 105–115.
- 568 (24) Prasad Saripalli, K.; McGrail, B.; Girvin, D. C. Adsorption of molybdenum on to
569 anatase from dilute aqueous solutions. *Applied Geochemistry* **2002**, *17*, 649–656.
- 570 (25) Goldberg, S. *Reference Module in Earth Systems and Environmental Sciences*; Elsevier,
571 2013.

- 572 (26) Liu, X.; Tournassat, C.; Grangeon, S.; Kalinichev, A. G.; Takahashi, Y.; Marques Fer-
573 nandes, M. Molecular-level understanding of metal ion retention in clay-rich materials.
574 *Nature Reviews Earth & Environment* **2022**, *3*, 461–476.
- 575 (27) Balistrieri, L. S.; Chao, T. Adsorption of selenium by amorphous iron oxyhydroxide
576 and manganese dioxide. *Geochimica et Cosmochimica Acta* **1990**, *54*, 739–751.
- 577 (28) Bickmore, B. R.; Tadanier, C. J.; Rosso, K. M.; Monn, W. D.; Eggett, D. L. Bond-
578 valence methods for pKa prediction: critical reanalysis and a new approach. *Geochimica
579 et Cosmochimica Acta* **2004**, *68*, 2025–2042.
- 580 (29) Zarzycki, P. Distance-dependent dielectric constant at the calcite/electrolyte interface:
581 Implication for surface complexation modeling. *Journal of Colloid and Interface Science*
582 **2023**, *645*, 752–764.
- 583 (30) Lee, S. S.; Fenter, P.; Park, C.; Sturchio, N. C.; Nagy, K. L. Hydrated Cation Speciation
584 at the Muscovite (001)-Water Interface. *Langmuir* **2010**, *26*, 16647–16651.
- 585 (31) Brinza, L.; Vu, H. P.; Neamtu, M.; Benning, L. G. Experimental and simulation results
586 of the adsorption of Mo and V onto ferrihydrite. *Scientific Reports* **2019**, *9*.
- 587 (32) Prange, M. P.; Mergelsberg, S. T.; Kerisit, S. N. Structural water in amorphous car-
588 bonate minerals: ab initio molecular dynamics simulations of X-ray pair distribution
589 experiments. *Physical Chemistry Chemical Physics* **2023**, *25*, 6768–6779.
- 590 (33) Kerisit, S.; Rosso, K. M. Charge transfer in FeO: A combined molecular-dynamics and
591 ab initio study. *The Journal of Chemical Physics* **2005**, *123*.
- 592 (34) Wang, S.; Zeng, X.; Lin, J.; Yuan, Z.; Qu, S.; Zhang, B.; Pan, Y.; Chen, N.; Chen, W.;
593 Jia, Y. Molecular Structure of Molybdate Adsorption on Goethite at pH 5–8: A Com-
594 bined DFT + U, EXAFS, and Ab Initio XANES Study. *The Journal of Physical Chem-
595 istry C* **2021**, *125*, 22052–22063.

- 596 (35) Davantès, A.; Costa, D.; Sallman, B.; Rakshit, S.; Lefèvre, G. Surface Polymerization of
597 Mo(VI) and W(VI) Anions on Hematite Revealed by in Situ Infrared Spectroscopy and
598 DFT+U Theoretical Study. *The Journal of Physical Chemistry C* **2016**, *121*, 324–332.
- 599 (36) Senftle, T. P.; Hong, S.; Islam, M. M.; Kylasa, S. B.; Zheng, Y.; Shin, Y. K.; Junker-
600 meier, C.; Engel-Herbert, R.; Janik, M. J.; Aktulga, H. M.; Verstraelen, T.; Grama, A.;
601 van Duin, A. C. T. The ReaxFF reactive force-field: development, applications and
602 future directions. *npj Computational Materials* **2016**, *2*.
- 603 (37) Pitman, M. C.; van Duin, A. C. T. Dynamics of Confined Reactive Water in Smectite
604 Clay-Zeolite Composites. *Journal of the American Chemical Society* **2012**, *134*, 3042–
605 3053.
- 606 (38) Huang, L.; Gubbins, K. E.; Li, L.; Lu, X. Water on Titanium Dioxide Surface: A
607 Revisiting by Reactive Molecular Dynamics Simulations. *Langmuir* **2014**, *30*, 14832–
608 14840.
- 609 (39) Manzano, H.; Moeini, S.; Marinelli, F.; van Duin, A. C. T.; Ulm, F.-J.; Pellenq, R. J.-
610 M. Confined Water Dissociation in Microporous Defective Silicates: Mechanism, Dipole
611 Distribution, and Impact on Substrate Properties. *Journal of the American Chemical
612 Society* **2012**, *134*, 2208–2215.
- 613 (40) Fogarty, J. C.; Aktulga, H. M.; Grama, A. Y.; van Duin, A. C. T.; Pandit, S. A. A
614 reactive molecular dynamics simulation of the silica-water interface. *The Journal of
615 Chemical Physics* **2010**, *132*.
- 616 (41) Nagata, Y.; Ohto, T.; Backus, E. H. G.; Bonn, M. Molecular Modeling of Water In-
617 terfaces: From Molecular Spectroscopy to Thermodynamics. *The Journal of Physical
618 Chemistry B* **2016**, *120*, 3785–3796.
- 619 (42) Hille, R.; Hall, J.; Basu, P. The Mononuclear Molybdenum Enzymes. *Chemical Reviews*
620 **2014**, *114*, 3963–4038.

- 621 (43) Giovannelli, D. Trace metal availability and the evolution of biogeochemistry. *Nature*
622 *Reviews Earth & Environment* **2023**, *4*, 597–598.
- 623 (44) Schwertmann, U.; Cornell, R. M. *Iron oxides in the laboratory: preparation and char-*
624 *acterization*; John Wiley & Sons, 2008.
- 625 (45) Michel, F. M.; Ehm, L.; Antao, S. M.; Lee, P. L.; Chupas, P. J.; Liu, G.; Stron-
626 gin, D. R.; Schoonen, M. A.; Phillips, B. L.; Parise, J. B. The structure of ferrihydrite,
627 a nanocrystalline material. *Science* **2007**, *316*, 1726–1729.
- 628 (46) Hiemstra, T. Surface and mineral structure of ferrihydrite. *Geochimica et Cosmochimica
629 Acta* **2013**, *105*, 316–325.
- 630 (47) Ong, S. P.; Richards, W. D.; Jain, A.; Hautier, G.; Kocher, M.; Cholia, S.; Gunter, D.;
631 Chevrier, V. L.; Persson, K. A.; Ceder, G. Python Materials Genomics (pymatgen):
632 A robust, open-source python library for materials analysis. *Computational Materials
633 Science* **2013**, *68*, 314–319.
- 634 (48) Thompson, A. P.; Aktulga, H. M.; Berger, R.; Bolintineanu, D. S.; Brown, W. M.;
635 Crozier, P. S.; in 't Veld, P. J.; Kohlmeyer, A.; Moore, S. G.; Nguyen, T. D.; Shan, R.;
636 Stevens, M. J.; Tranchida, J.; Trott, C.; Plimpton, S. J. LAMMPS - a flexible simulation
637 tool for particle-based materials modeling at the atomic, meso, and continuum scales.
638 *Comp. Phys. Comm.* **2022**, *271*, 108171.
- 639 (49) Aktulga, H. M.; Fogarty, J. C.; Pandit, S. A.; Grama, A. Y. Parallel reactive molecular
640 dynamics: Numerical methods and algorithmic techniques. *parallel computing* **2012**,
641 *38*, 245–259.
- 642 (50) Aryanpour, M.; van Duin, A. C.; Kubicki, J. D. Development of a reactive force field
643 for iron- oxyhydroxide systems. *The Journal of Physical Chemistry A* **2010**, *114*, 6298–
644 6307.

- 645 (51) Chenoweth, K.; Van Duin, A. C.; Goddard III, W. A. The ReaxFF Monte Carlo reactive
646 dynamics method for predicting atomistic structures of disordered ceramics: application
647 to the Mo₃VO_x Catalyst. *Angewandte Chemie International Edition* **2009**, *48*, 7630–
648 7634.
- 649 (52) Fedkin, M. V.; Shin, Y. K.; Dasgupta, N.; Yeon, J.; Zhang, W.; van Duin, D.; van
650 Duin, A. C. T.; Mori, K.; Fujiwara, A.; Machida, M.; Nakamura, H.; Okumura, M.
651 Development of the ReaxFF Methodology for Electrolyte–Water Systems. *The Journal
652 of Physical Chemistry A* **2019**, *123*, 2125–2141.
- 653 (53) Ta, T. D.; Le, H. M.; Tieu, A. K.; Zhu, H.; Ta, H. T. T.; Tran, N. V.; Wan, S.; van
654 Duin, A. Reactive Molecular Dynamics Study of Hierarchical Tribocatalytic Lubricant
655 Films at Elevated Temperatures. *ACS Applied Nano Materials* **2020**, *3*, 2687–2704.
- 656 (54) Kohlmeyer, A.; Vermaas, J. TopoTools, Release 1.9. 2022.
- 657 (55) Jewett, A. I.; Stelter, D.; Lambert, J.; Saladi, S. M.; Roscioni, O. M.; Ricci, M.;
658 Autin, L.; Maritan, M.; Bashusqeh, S. M.; Keyes, T., et al. Moltemplate: A tool
659 for coarse-grained modeling of complex biological matter and soft condensed matter
660 physics. *Journal of molecular biology* **2021**, *433*, 166841.
- 661 (56) Rappe, A. K.; Goddard III, W. A. Charge equilibration for molecular dynamics simu-
662 lations. *The Journal of Physical Chemistry* **1991**, *95*, 3358–3363.
- 663 (57) Martínez, L.; Andrade, R.; Birgin, E. G.; Martínez, J. M. PACKMOL: A package for
664 building initial configurations for molecular dynamics simulations. *Journal of compu-
665 tational chemistry* **2009**, *30*, 2157–2164.
- 666 (58) Azenha, M.; Szefczyk, B. Exploration of the reactive modelling of sol–gel polyconden-
667 sation in the presence of templates. *Soft Matter* **2019**, *15*, 5770–5778.

- 668 (59) Gowers, R.; Linke, M.; Barnoud, J.; Reddy, T.; Melo, M.; Seyler, S.; Domański, J.;
669 Dotson, D.; Buchoux, S.; Kenney, I.; Beckstein, O. MDAnalysis: A Python Package for
670 the Rapid Analysis of Molecular Dynamics Simulations. Proceedings of the Python in
671 Science Conference. 2016.
- 672 (60) Michaud-Agrawal, N.; Denning, E. J.; Woolf, T. B.; Beckstein, O. MDAnalysis: A
673 toolkit for the analysis of molecular dynamics simulations. *Journal of Computational*
674 *Chemistry* **2011**, *32*, 2319–2327.
- 675 (61) Kästner, J. Umbrella sampling. *WIREs Computational Molecular Science* **2011**, *1*,
676 932–942.
- 677 (62) Fiorin, G.; Klein, M. L.; Hénin, J. Using collective variables to drive molecular dynamics
678 simulations. *Molecular Physics* **2013**, *111*, 3345–3362.
- 679 (63) Kumar, S.; Rosenberg, J. M.; Bouzida, D.; Swendsen, R. H.; Kollman, P. A. Mul-
680 tidimensional free-energy calculations using the weighted histogram analysis method.
681 *Journal of Computational Chemistry* **1995**, *16*, 1339–1350.
- 682 (64) Grossfield, A. WHAM: the weighted histogram analysis method, version 2.0.10.1. *Avail-
683 able at membrane. urmc. rochester. edu/content/wham. Accessed November 2023*,
- 684 (65) Toby, B. H.; Dreele, R. B. V. GSAS-II: the genesis of a modern open-source all purpose
685 crystallography software package. *Journal of Applied Crystallography* **2013**, *46*, 544–
686 549.
- 687 (66) Waasmaier, D.; Kirfel, A. New analytical scattering-factor functions for free atoms
688 and ions. *Acta Crystallographica Section A: Foundations of Crystallography* **1995**, *51*,
689 416–431.
- 690 (67) Larsen, A. H. et al. The atomic simulation environment—a Python library for working
691 with atoms. *Journal of Physics: Condensed Matter* **2017**, *29*, 273002.

- 692 (68) Juhás, P.; Farrow, C. L.; Yang, X.; Knox, K. R.; Billinge, S. J. L. Complex modeling:
693 a strategy and software program for combining multiple information sources to solve ill
694 posed structure and nanostructure inverse problems. *Acta Crystallographica Section A*
695 *Foundations and Advances* **2015**, *71*, 562–568.
- 696 (69) Michel, F. M. et al. Similarities in 2- and 6-Line Ferrihydrite Based on Pair Distribution
697 Function Analysis of X-ray Total Scattering. *Chemistry of Materials* **2007**, *19*, 1489–
698 1496.
- 699 (70) Michel, F. M.; Ehm, L.; Antao, S. M.; Lee, P. L.; Chupas, P. J.; Liu, G.; Strongin, D. R.;
700 Schoonen, M. A. A.; Phillips, B. L.; Parise, J. B. The Structure of Ferrihydrite, a
701 Nanocrystalline Material. *Science* **2007**, *316*, 1726–1729.
- 702 (71) Liu, W.; Etschmann, B.; Mei, Y.; Guan, Q.; Testemale, D.; Brugger, J. The role of sulfur
703 in molybdenum transport in hydrothermal fluids: Insight from in situ synchrotron XAS
704 experiments and molecular dynamics simulations. *Geochimica et Cosmochimica Acta*
705 **2020**, *290*, 162–179.
- 706 (72) Johansson, G.; Caminiti, R. The Hydration of Tungstate and Molybdate Ions in Aque-
707 ous Solution. *Zeitschrift für Naturforschung A* **1986**, *41*, 1325–1329.
- 708 (73) Harrington, R.; Hausner, D. B.; Bhandari, N.; Strongin, D. R.; Chapman, K. W.;
709 Chupas, P. J.; Middlemiss, D. S.; Grey, C. P.; Parise, J. B. Investigation of Surface
710 Structures by Powder Diffraction: A Differential Pair Distribution Function Study on
711 Arsenate Sorption on Ferrihydrite. *Inorganic Chemistry* **2009**, *49*, 325–330.
- 712 (74) Zhang, J.; Wang, S.; Ma, X.; Yao, S.; Lv, H.; Pan, Y.; Chernikov, R.; Heredia, E.;
713 Lin, J.; Jia, Y. Observation of surface precipitation of ferric molybdate on ferrihydrite:
714 Implication for the mobility and fate of molybdate in natural and hydrometallurgical
715 environments. *Science of The Total Environment* **2022**, *807*, 150749.

- 716 (75) Appelo, C. A. J.; Weiden, M. J. J. V. D.; Tournassat, C.; Charlet, L. Surface Complex-
717 ation of Ferrous Iron and Carbonate on Ferrihydrite and the Mobilization of Arsenic.
718 *Environmental Science & Technology* **2002**, *36*, 3096–3103.
- 719 (76) Lee, S. S.; Koishi, A.; Bourg, I. C.; Fenter, P. Ion correlations drive charge overscreening
720 and heterogeneous nucleation at solid–aqueous electrolyte interfaces. *Proceedings of the
721 National Academy of Sciences* **2021**, *118*.
- 722 (77) Sassi, M.; Chaka, A. M.; Rosso, K. M. Ab initio thermodynamics reveals the nanocom-
723 posite structure of ferrihydrite. *Communications Chemistry* **2021**, *4*.
- 724 (78) Kurapothula, P. K. J.; Shepherd, S.; Wilkins, D. M. Competing Nuclear Quantum
725 Effects and Hydrogen-Bond Jumps in Hydrated Kaolinite. *The Journal of Physical
726 Chemistry Letters* **2023**, *14*, 1542–1547.
- 727 (79) Piana, S.; Jones, F.; Gale, J. D. Assisted Desolvation as a Key Kinetic Step for Crystal
728 Growth. *Journal of the American Chemical Society* **2006**, *128*, 13568–13574.
- 729 (80) Pokora, M.; Paneth, A.; Paneth, P. Non-Covalent Isotope Effects. *The Journal of Phys-
730 ical Chemistry Letters* **2023**, *14*, 3735–3742.
- 731 (81) Muthachikavil, A. V.; Peng, B.; Kontogeorgis, G. M.; Liang, X. Distinguishing Weak
732 and Strong Hydrogen Bonds in Liquid Water—A Potential of Mean Force-Based Ap-
733 proach. *The Journal of Physical Chemistry B* **2021**, *125*, 7187–7198.
- 734 (82) Kański, M.; Hrabar, S.; van Duin, A. C. T.; Postawa, Z. Development of a Charge-
735 Implicit ReaxFF for C/H/O Systems. *The Journal of Physical Chemistry Letters* **2022**,
736 *13*, 628–633.
- 737 (83) Shultz, M. J.; Bisson, P.; Vu, T. H. Insights into hydrogen bonding via ice interfaces
738 and isolated water. *The Journal of Chemical Physics* **2014**, *141*.

- 739 (84) Norén, K.; Persson, P. Adsorption of monocarboxylates at the water/goethite interface:
740 The importance of hydrogen bonding. *Geochimica et Cosmochimica Acta* **2007**, *71*,
741 5717–5730.
- 742 (85) Zhao, K.; Chang, X.; Su, H.; Nie, Y.; Lu, Q.; Xu, B. Enhancing Hydrogen Oxidation
743 and Evolution Kinetics by Tuning the Interfacial Hydrogen Bonding Environment on
744 Functionalized Platinum Surfaces. *Angewandte Chemie* **2022**, *134*.
- 745 (86) Zhang, W.; van Duin, A. C. T. Second-Generation ReaxFF Water Force Field: Im-
746 provements in the Description of Water Density and OH-Anion Diffusion. *The Journal*
747 *of Physical Chemistry B* **2017**, *121*, 6021–6032.
- 748 (87) Lammers, L. N.; Kulasinski, K.; Zarzycki, P.; DePaolo, D. J. Molecular simulations of
749 kinetic stable calcium isotope fractionation at the calcite-aqueous interface. *Chemical*
750 *Geology* **2020**, *532*, 119315.
- 751 (88) Schmidt, M. P.; Siciliano, S. D.; Peak, D. Spectroscopic Quantification of Inner- and
752 Outer-Sphere Oxyanion Complexation Kinetics: Ionic Strength and Background Cation
753 Effect on Sulfate Adsorption to Hematite. *ACS Earth and Space Chemistry* **2020**, *4*,
754 1765–1776.
- 755 (89) Bourg, I. C.; Lee, S. S.; Fenter, P.; Tournassat, C. Stern Layer Structure and Energetics
756 at Mica-Water Interfaces. *The Journal of Physical Chemistry C* **2017**, *121*, 9402–9412.
- 757 (90) Leung, K.; Criscenti, L. J. Predicting the acidity constant of a goethite hydroxyl group
758 from first principles. *Journal of Physics: Condensed Matter* **2012**, *24*, 124105.
- 759 (91) Leung, K.; Nielsen, I. M. B.; Criscenti, L. J. Elucidating the Bimodal Acid-Base Be-
760 havior of the Water-Silica Interface from First Principles. *Journal of the American*
761 *Chemical Society* **2009**, *131*, 18358–18365.

762 (92) Dzombak, D. A.; Morel, F. M. *Surface complexation modeling: hydrous ferric oxide*;
763 John Wiley & Sons, 1991.

764 (93) Ferrari, C.; Resongles, E.; Freydier, R.; Casiot, C. Antimony isotope fractionation
765 during Sb(V) and Sb(III) adsorption on secondary Fe-minerals (schwertmannite, ferri-
766 hydrite) typical of mine waters. *Applied Geochemistry* **2024**, *163*, 105935.